Formulation and Emulation of Quantum-Inspired Dynamical Systems With Classical Analog Circuits

ARTICLE **Communicated by Gert Cauwenberghs**

Formulation and Emulation of Quantum-Inspired Dynamical Systems With Classical Analog Circuits

A. J. Cressman
anthony.j.cressman.gr@dartmouth.edu
Department of Physics, Dartmouth College, Hanover, NH 03755, U.S.A.

W. Wattanapanitch
woradorn@gmail.com
Department of Electrical Engineering, Kasetsart University, Bangkok 10900, Thailand

I. Chuang
ichuang@mit.edu
Departments of Electrical Engineering and Physics, MIT, Cambridge, MA 02139, U.S.A.

R. Sarpeshkar
rahul.sarpeshkar.dartmouth@gmail.com
Departments of Engineering, Physics, Microbiology and Immunology, and Molecular and Systems Biology, Dartmouth College, Hanover, NH 03755, U.S.A.

Quantum dynamical systems are capable of powerful computation but are hard to emulate on digital computers. We show that four novel analog circuit parts can emulate the phase-coherent unitary dynamics of such systems. These four parts are: a Planck capacitance analogous to a neuronal membrane capacitance; a quantum admittance element, together with the Planck capacitance, analogous to a neuronal quadrature oscillator; a quantum transadmittance element analogous to a complex neuronal synapse; and a quantum transadmittance mixer element analogous to a complex neuronal synapse with resonant modulation. These parts may be emulated classically, with paired real-value voltages on paired Planck capacitances corresponding to the real and imaginary portions of a probability amplitude; and appropriate paired real-value currents onto these Planck capacitances corresponding to diagonal (admittance), off-diagonal (transadmittance), or controlled off-diagonal (transadmittance mixer) Hamiltonian energy terms. The superposition of 2^n simultaneously phase-coherent and symmetric probability-voltage amplitudes with $O(n)$ of these parts, in a tensor-product architecture enables analog emulation of the quantum Fourier transform (QFT). Implementation

R. Sarpeshkar is the corresponding author.

Neural Computation **34, 856–890** (2022)
https://doi.org/10.1162/neco_a_01481

of our circuits on an analog integrated circuit in a 0.18 μm process yield experimental results consistent with mathematical theory and computer simulations for emulations of NMR, Josephson junction, and QFT dynamics. Our results suggest that linear oscillatory neuronal networks with pairs of complex subthreshold/nonspiking sine and cosine neurons that are coupled together via complex synapses to other such complex neurons can architect quantum-inspired computation with classical analog circuits. Thus, an analog-circuit mapping between quantum and neural computation, both of which exploit analog computation for powerful operation, can enable future synergies between these fields.

1 Introduction

Feynman first described the powerful computational possibilities inherent in the physics of coherent wave interference as well as the ability of quantum dynamical systems to emulate quantum physics efficiently (Feynman, 1982; Nielsen & Chuang, 2010). Efficient simulation of hard problems in quantum mechanics can sometimes be accomplished with more conventional means. Often the efficiency comes from a physical system, such as linear optics, designed to evolve in similar ways to the quantum system in question (Cohen et al., 2021). An advantage of such physical emulation is that it can be designed to inherently take advantage of coherent feedback dynamics or probabilistic computation with noise, both of which are automatically present in the physical system. Such systems also have applications in fields such as machine learning, which is largely founded on neural computation (Yamamoto, Leleu, Ganguli, & Mabuchi, 2020).

Analog accelerators for linear algebra have been shown to be capable of order-of-magnitude improvements over digital computation (Huang, Guo, Seok, Tsividis, & Sethumadhavan, 2016). Analog circuits can be used to exploit the stochastic nature of the behavior of electrons at different energy barriers, which is normally avoided in other applications (Fukami et al., 2020). Probabilistic computation with natural thermal noise in thermodynamic analog computers enables vast speed-ups for emulating biological stochastic computation and can also solve problems like integer factorization (Kim, Woo, & Sarpeshkar, 2018; Borders et al., 2019). Powerful analog computational basis functions were identified to have benefits for emulating neuron-inspired computation in the brain and for pattern recognition (Mead, 1989; Hahnloser, Sarpeshkar, Mahowald, Douglas, & Seung, 2000; Lee & Seung, 1999). Similarly, novel physical devices like memristors can emulate short-term and long-term synaptic plasticity in the brain (Wang et al., 2017). The nature of measurement and causality can be explored with loaded alternating current (AC) circuits (Weinstein, 2021). Finally, quantum information processing in conventional commercial integrated circuits can be enabled in the future by elegant techniques for single-electron

spin-to-charge conversion and detection (Xiao, Martin, Yablonovitch, & Jiang, 2004).

All of this prior work suggests that physical collective analog computation, whether probabilistic or deterministic, classical or quantum, is a powerful alternative to traditional digital computation. It is also readily available in commercial integrated circuits at room temperature. In particular, the power of using unitary transforms that exploit phase to compute, such as the quantum Fourier transform (QFT), has applications in many domains. Examples include search (Grover, 1996), quantum chemistry simulations (Whitfield, Biamonte, & Aspuru-Guzik, 2011), and integer factorization (Shor, 1994). It is worth noting that unlike traditional analog computation, collective analog computation is scalable to arbitrary complexity and precision because global-function discrete outcomes or digitization enable signal restoration and divide-and-conquer computation (Nielsen & Chuang, 2010; Sarpeshkar, 1998, 2010; Woo & Sarpeshkar, 2013). For example, it is possible to do 16-bit-precise (or arbitrarily precise) analog addition with four 4-bit-precise spiking-neuron analog units using physical basis functions of Kirchoff's current law and the mechanism of a signal-restorative pulsatile spiking carry rather than via traditional full-adder digital logic (Woo & Sarpeshkar, 2013). Such spiking-neuron circuits are capable of powerful arbitrary general-purpose computation, from generalizations of synchronous finite state machines in the digital domain to asynchronous hybrid state machines in the spiking domain, and are also capable of learning (Sarpeshkar & O'Halloran, 2002). Emulating coherent quantum computation with classical analog circuits over a broadband, scalable frequency range is difficult; to be unitary, one must conserve energy, which is satisfied by approximately lossless passive inductor-capacitor circuits that can renormalize their signals to account for small loss. However, the magnitude-phase relationships of such circuits at just one narrow resonant frequency are not sufficient for them to correctly emulate quantum dynamics at all frequencies. When such circuits are composed together to emulate quantum mechanics over a broadband frequency range, nonmodular, current-voltage interactions due to the interacting effects of one circuit on another alter the quantum computation being emulated. The circuit is neither broadband as it is required to be nor easily scalable due to such loading and associated frequency-dependent interactions.

Perfect -90° phase shifts are required over a broad frequency range to represent the complex number i in classical analog dynamical systems when emulating quantum dynamical systems (Kish, 2003; La Cour, Ostrove, Ott, Starkey, & Wilson, 2016). Unfortunately, such perfect phase shifts with no magnitude change are physically impossible to architect by real-voltage, real-current single-element classical circuits over all frequencies. They need an infinite number of lumped classical circuit elements to emulate (Sarpeshkar, 2019a, 2019b, 2019c, 2020). Coherent unitary quantum computation needs fundamentally new analog circuits that represent its

complex-number mathematics with complex-voltage/complex-current circuits. These circuits have no direct real-voltage/real-current classical equivalent. Furthermore, even narrowband emulations of quantum dynamics need exponential hardware resources to mimic the tensor-product properties of quantum computing (Kish, 2003). Active real-valued classical analog circuits seem ill suited for emulating unitary quantum computation because they do not inherently conserve energy like passive circuits. However, we show that one passive and three active complex-valued quantum analog circuits can conserve both probability and energy and implement unitary transforms. These four parts can reformulate the Hamiltonian equations of quantum mechanics in a circuits language that is easily scalable, broadband, and modular. They can be used together to compose tensor-product systems that do not require exponential resources in hardware. Most important, although these parts with complex voltages and complex currents have no direct classical equivalent, we can emulate these four parts classically using only real-valued voltages and currents. Alternatively, complex neurons with paired sine and cosine quadrature oscillations that interact via a complex Hamiltonian synaptic matrix can classically emulate powerful aspects of quantum computation, thus building a circuit bridge between quantum and neural computation. Both of these forms of computation exploit analog computation, whether with complex numbers or with real numbers, respectively.

Recent work (Budzinski et al., 2021) on using complex numbers to more clearly understand coupled oscillations in nonlinear systems (Kuramoto, 1984) via a more linear framework is in accord with our complementary work here. As we show, it is consistent with our measurements and emulations of reactive power-flow currents in Josephson junction emulations. Other recent work has shown that quantum spin-based Ising systems, including probability distributions corresponding to those seen in quantum entanglement, can be learned and emulated by networks of leaky integrate-and-fire spiking neurons on VLSI chips. These implementations effectively architect positive operator-valued measures (Czischek et al., 2021). Our work is complementary and consistent with such work since we effectively architect linear, nonspiking classical analog quadrature oscillator circuits to represent phase. In contrast, spiking systems can architect modular representations of real numbers by effectively encoding 0° phase at the spike onset (Sarpeshkar & O'Halloran, 2002).

2 Emulation of Quantum Hamiltonian Dynamics with Classical Analog Circuits

We start by showing how we can emulate the coherent dynamics of quantum dynamical systems classically. We observe that quantum complex-valued analog computation naturally maps to classical paired-real-value analog computation if we make one simple but critical observation: Since

$-i(R + iI) = -iR + I$, the Schrodinger equation, $\hbar d|\psi\rangle/dt = -iH|\psi\rangle$, always leads to real-valued components in $H|\psi\rangle$ creating imaginary-valued dynamic components in $d|\psi\rangle/dt$ with a sign change and imaginary-valued components in $H|\psi\rangle$ creating real-valued dynamic components in $d|\psi\rangle/dt$ with no sign change. Thus, if we keep separate track of the real and imaginary components and their interacting dynamics, an $N \times N$ quantum Hamiltonian that is Hermitian with N complex-valued state variables maps to an equivalent classical analog $2N \times 2N$ Hamiltonian. This Hamiltonian is anti-Hermitian with $2N$ paired real-value (R, I) state variables. In general, because $i^2 = -1$ and real and imaginary parts always reciprocally affect each other, quantum complex dynamics always manifests with equivalent paired-real-value classical variables that interact via active negative-feedback loops. Equivalently, there are always two corresponding dual dynamical systems that interact. Below, we prove that a real eigenvalue, E_0, of a quantum Hermitian system with an $N \times 1$ eigenvector $|\psi\rangle$ transforms to a pair of eigenvalues, $-iE_0$ and $+iE_0$, with corresponding $2N \times 1$ eigenvectors of an equivalent classical anti-Hermitian system, which are denoted by $|\psi; -i\psi\rangle$ and $|\psi^*; +i\psi^*\rangle$, respectively. These eigenvectors naturally sum in complex-conjugate fashion to create real-valued classical analog dynamics, analogous but not always equal to cosine and sine components of the exactly emulated complex exponential quantum dynamics. Hermitian Hamiltonian dynamics, which conserve probability and energy in quantum systems, map to corresponding anti-Hermitian Hamiltonian dynamics in our classical emulations, which conserve energy and power, respectively, making unitary transforms realizable.

The quantum Schrodinger equation, which is intentionally rewritten such that $\hbar$ can be mapped to a Planck capacitance in our emulations (i.e., i has been moved to the right-hand side), may be written as

$$\hbar \frac{\mathrm{d}}{\mathrm{d}t}|\psi\rangle = -iH|\psi\rangle.$$

If we separate the probability amplitude and Hamiltonian into real and imaginary parts (here using superscripts R and I for real and imaginary parts, respectively),

$$\hbar \frac{\mathrm{d}}{\mathrm{d}t}\left(|\psi^R\rangle + i|\psi^I\rangle\right) = -i(H^R + iH^I)\left(|\psi^R\rangle + i|\psi^I\rangle\right)$$

$$\Longrightarrow \hbar \frac{\mathrm{d}}{\mathrm{d}t}\begin{bmatrix}\psi^R \\ \psi^I\end{bmatrix} = \begin{bmatrix} H^I & H^R \\ -H^R & H^I\end{bmatrix}\begin{bmatrix}\psi^R \\ \psi^I\end{bmatrix}.$$

We can then see how an $N \times N$ quantum Hamiltonian with complex numbers has been mapped to an equivalent $2N \times 2N$ classical Hamiltonian with real numbers and an N-dimensional complex state vector has been

mapped to an equivalent $2N$-dimensional classical state vector with real numbers.

We now discuss how the eigenvalues and eigenvectors of the classical Hamiltonian, which is anti-Hermitian, relate to the eigenvalues and eigenvectors of the quantum Hamiltonian, which is Hermitian. Suppose that $|E_i\rangle$ is an eigenvector of the quantum Hermitian Hamiltonian with eigenvalue E_i. Then,

$$i\hbar\frac{\mathrm{d}}{\mathrm{d}t}|E_i\rangle = H|E_i\rangle = E_i|E_i\rangle.$$

And by taking complex conjugates of each side,

$$-i\hbar\frac{\mathrm{d}}{\mathrm{d}t}|E_i^*\rangle = H^*|E_i^*\rangle = E_i|E_i^*\rangle.$$

Therefore, in the classical Hamiltonian,

$$\begin{bmatrix} H^I & H^R \\ -H^R & H^I \end{bmatrix}\begin{bmatrix} |E_i\rangle \\ -i|E_i\rangle \end{bmatrix} = \begin{bmatrix} -iH|E_i\rangle \\ -H|E_i\rangle \end{bmatrix} = -iE_i\begin{bmatrix} |E_i\rangle \\ -i|E_i\rangle \end{bmatrix},$$

such that the latter vector in the equation above is an eigenvector of the classical Hamiltonian with eigenvalue $-iE_i$.

Similarly,

$$\begin{bmatrix} H^I & H^R \\ -H^R & H^I \end{bmatrix}\begin{bmatrix} |E_i^*\rangle \\ i|E_i^*\rangle \end{bmatrix} = \begin{bmatrix} iH^*|E_i^*\rangle \\ -H^*|E_i^*\rangle \end{bmatrix} = iE_i\begin{bmatrix} |E_i^*\rangle \\ i|E_i^*\rangle \end{bmatrix},$$

such that the latter vector in the equation above is an eigenvector of the classical Hamiltonian with eigenvalue $+iE_i$. Thus, we have a homomorphism with a single E_i quantum eigenvalue and associated eigenvector mapping to two classical $-iE_i$ and $+iE_i$ eigenvectors with associated eigenvectors.

It is worth noting that as for all ordinary oscillators in classical systems, the eigenvectors for each eigenvalue sum with their complex-conjugate halves (with appropriate initial-condition weighting that also turns out to be complex conjugate) throughout the dynamics to yield values for each real and imaginary component that is real-valued. Therefore, these components are physically instantiable, classically, as our experiments and theory show. An example that bears strong similarity and provides intuition is that

right-hand, circularly polarized (RHCP) $e^{i\omega t}$ and left-hand, circularly polarized (LHCP) $e^{i\omega t}$ components sum in complex-conjugate fashion to create linearly polarized cosine and sine components on the x- and y-axes.

If we replace the H^R and H^I terms with G^R and G^I complex admittance terms (complex admittance = complex current/complex voltage), circuit dynamics of probability amplitude voltages across Planck capacitors whose value is $\hbar$ can represent quantum Hamiltonian dynamics:

$$C_\hbar \frac{\mathrm{d}}{\mathrm{d}t}\begin{bmatrix} V^R \\ V^I \end{bmatrix} = \begin{bmatrix} I^R \\ I^I \end{bmatrix} = \begin{bmatrix} G^I & G^R \\ -G^R & G^I \end{bmatrix}\begin{bmatrix} V^R \\ V^I \end{bmatrix}.$$

Here, V^R and V^I are vectors with N real components. The G matrix represents admittances connected to these Planck capacitors in an appropriate feedback fashion as we show later. Note that our G matrix is itself antisymmetric, and the conjugate transpose is simply the transpose in this formulation $G^T = -G$. One can see this more clearly by looking at G in a factored form:

$$\begin{aligned} -i\left(G^R + iG^I\right)\left(|V^R\rangle + i|V^I\rangle\right) &= \left(G^I|V^R\rangle + G^R|V^I\rangle\right) + i\left(-G^R|V^R\rangle + G^I|V^I\rangle\right) \\ &= \begin{bmatrix} G^I & G^R \\ -G^R & G^I \end{bmatrix}\begin{bmatrix} V^R \\ V^I \end{bmatrix} \\ \Longrightarrow \left[-i\left(G^R + iG^I\right)\right]^\dagger &= +i\left(\left(G^R\right)^T - i\left(G^I\right)^T\right) \\ &= +i\left(G^R + iG^I\right) \\ &= \begin{bmatrix} -G^I & -G^R \\ G^R & -G^I \end{bmatrix}. \end{aligned}$$

While this arrangement of the real and imaginary parts (real parts stacked on imaginary parts) is useful in this context, it is sometimes more convenient to alternate real and imaginary parts (e.g., $|V\rangle = \begin{bmatrix} V_1^R & V_1^I & V_2^R & V_2^I \end{bmatrix}^T$), which better illustrates the connections between real-imaginary pairs of different Planck capacitors. Figure 1 illustrates how a simple 2×2 quantum Hamiltonian is then mapped to an equivalent classical 4×4 Hamiltonian.

For later convenience, we note that

$$\begin{aligned} C_\hbar \frac{\mathrm{d}}{\mathrm{d}t}|V\rangle &= |I\rangle = G|V\rangle \\ \frac{\mathrm{d}}{\mathrm{d}t}|V\rangle &= \frac{1}{C_\hbar}G|V\rangle \\ \frac{\mathrm{d}}{\mathrm{d}t}|I\rangle &= \frac{1}{C_\hbar}G^2|V\rangle. \end{aligned}$$

$$H = \begin{bmatrix} E_1 & -A \\ -A^* & E_2 \end{bmatrix} \qquad H_c = \begin{bmatrix} 0 & E_1 & -A^I & -A^R \\ -E_1 & 0 & A^R & -A^I \\ A^I & -A^R & 0 & E_2 \\ A^R & A^I & -E_2 & 0 \end{bmatrix}$$

Quantum Hamiltonian Classical Hamiltonian

Figure 1: A quantum Hamiltonian can be simply mapped to an equivalent classical Hamiltonian.

3 Four Classical Analog Circuit Components to Emulate Quantum Dynamics

We have described how a quantum Hamiltonian can be emulated by equivalent classical circuit dynamics. To review, quantum complex-valued analog computation naturally maps to classical paired-real-value analog computation if we make one simple but critical observation, since, $-i(R + iI) = iR + I$, the Schrodinger equation, $\hbar d|\psi\rangle/dt = -iH|\psi\rangle$, always leads to real-valued components in $H|\psi\rangle$, creating imaginary-valued dynamic components in $d|\psi\rangle/dt$ with a sign change and imaginary-valued components in $H|\psi\rangle$ creating real-valued dynamic components in $d|\psi\rangle/dt$ with no sign change. Thus, complex currents that flow onto what we call $\hbar$ Planck capacitors (whose voltage represents probability amplitude) can architect probability-amplitude component changes on these capacitors and represent changing dynamics of the quantum system. Each complex probability-amplitude voltage component in the quantum Hamiltonian can, in general, architect diagonal or self-dynamics by generating currents that are fed to its own Planck capacitors (via what we term a "quantum admittance" element that corresponds to the E_1 term in Figure 1) or architect off-diagonal or trans dynamics by generating currents that are fed to other Planck capacitors (via what we term a "complex transadmittance" element that corresponds to the A term in Figure 1). Controlled off-diagonal interactions can be implemented via what we term a "quantum transadmittance mixer" element, for example, if A in Figure 1 is modulated by another input.

We now describe these four circuit components in more detail. They can serve as the building blocks for larger circuits. Later, we also show how they can be used in a superposition context, analogous to the signal representation described in La Cour et al. (2016) but with $O(n)$ scaling in hardware resources for our tensor-product architecture that leverages symmetry useful in the QFT and in several quantum algorithms, rather than $O(2^n)$ for the arbitrary case.

3.1 Planck Capacitor. A complex voltage on a Planck capacitor can represent a single probability-amplitude component and be emulated by a pair

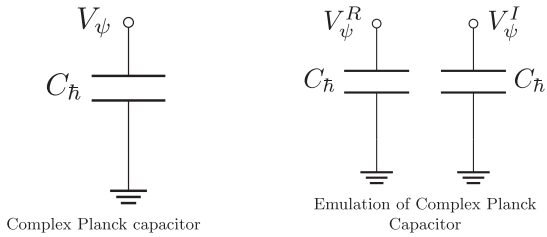

Figure 2: The complex Planck capacitor (which has no physical realization) can be emulated with a pair of capacitors for the real and imaginary components.

of voltages on two identical classical capacitors, as shown in Figure 2. Since the capacitance naturally represents $\hbar$, we refer to this component as the "Planck capacitor." We use the capacitor symbol in all circuit drawings. This capacitance, analogous to the neuronal membrane capacitance, scales all dynamics in inverse proportion to its capacitance value.

3.2 Quantum Admittance Element. A diagonal self-dynamical term of the quantum Hamiltonian is represented via a quantum admittance element that creates a current $I_E = -iG_E V_E$ representing an E_i term of the quantum Hamiltonian with G_E, the admittance/transconductance proportional to E_i. The physical instantiation in the classical emulation leads to $I_E^R = G_E V_E^I$ and $I_E^I = -G_E V_E^R$ with such currents altering the voltages V_E^R and V_E^I on the Planck capacitances $C_\hbar$ that they are implicitly connected to (these Planck capacitances are like those explicitly shown in Figure 2). We note that the transconductance values relate to the energy values E_1 and E_2 from Figure 1. We have introduced a new symbol for this element (see Figure 3). Figure 4 shows a simple implementation of this element.

3.3 Complex Transadmittance Element. An off-diagonal transdynamical term of the quantum Hamiltonian is represented via a quantum transadmittance element that creates a current $I_o = -i(-G_A)V_I$ representing an $-A$ or $-A^*$ term of the quantum Hamiltonian with G_A, the transadmittance proportional to A (or A^*). The physical instantiation in the classical emulation leads to $I_o^R = -G_A V_{in}^I$ and $I_o^I = G_A V_{in}^R$ if A is purely real with such currents altering the voltages V_o^R and V_o^I on the Planck capacitances $C_\hbar$ that they are connected to, which are different from the input voltages to the element, V_{in}^R and V_{in}^I. The physical instantiation in the classical emulation leads to $I_o^R = -G_A V_{in}^R$ and $I_o^I = -G_A V_{in}^I$ if A is purely imaginary with such currents altering the voltages V_o^R and V_o^I on the Planck capacitances $C_\hbar$ that they are connected to, which are different from the input voltages to the elements, V_{in}^R and V_{in}^I. The signs of these currents are consistent with the classical Hamiltonian of Figure 1, which is also derived by keeping track of

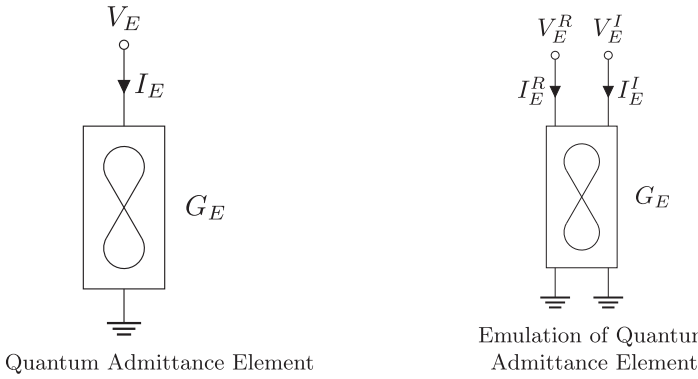

Figure 3: The complex quantum admittance element can be emulated with an element that takes the real and imaginary parts as separate inputs. The resulting current is $I_E = -iG_E V_E$.

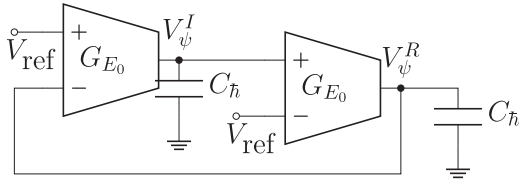

Figure 4: A simple implementation of the quantum admittance element using two transconductance amplifiers in feedback with each other (Sarpeshkar, 2019a, 2019b, 2019c, 2020).

real and imaginary components. Internally they can be realized as voltage-controlled current sources with simple multipliers and adders to facilitate complex multiplication. We introduce a new symbol for this element as well (see Figure 5).

3.4 Complex Transadmittance Mixer Element. An off-diagonal transdynamical term of the quantum Hamiltonian is represented via a quantum transadmittance mixer element that creates a current $I_o = -i(-G_A)V_1V_2$) representing complex mixing of two inputs V_1 and V_2 that leads to a complex output current I_o. The physical instantiation in the classical emulation leads to $I_o^R = -G_A(V_1^R V_2^I + V_1^I V_2^R)$ and $I_o^I = +G_A(V_1^R V_2^R - V_1^I V_2^I)$. This part enables emulation of off-diagonal interactions corresponding to a time-dependent control input (Feynman, Leighton, & Sands, 2011), for example, in atoms interacting with light, in NMR physics, in universal controlled-NOT quantum gates (Nielsen & Chuang, 2010), and in the QFT. It is

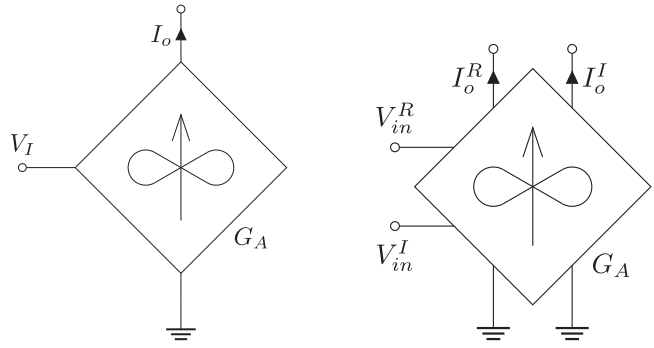

Complex Transadmittance Element

Emulation of Complex Transadmittance Element

Figure 5: The complex transadmittance element can be emulated with an element that takes the real and imaginary parts as separate inputs. A simple implementation can be had with voltage-controlled current sources that add appropriately to perform complex multiplication (complex G_A multiplying complex V_I as in Sarpeshkar, 2019a, 2019b, 2019c, 2020). The resulting current is $I_o = -i(-G_A)V_I$.

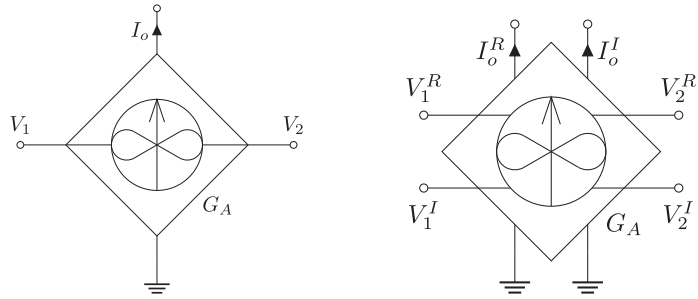

Complex Transadmittance Mixer Element

Emulation of Complex Transadmittance Mixer Element

Figure 6: The complex transadmittance element can be emulated with an element that takes separate real and imaginary parts. The mixer first multiplies the two input signal voltages (using complex multiplication as in Sarpeshkar, 2019a, 2019b, 2019c, 2020) before scaling the current by G_A, which may be complex. The resulting current is $I_o = -i(-G_A)V_1V_2$.

also analogous to a complex neuronal synapse with a complex resonant modulating input. The symbol we use for this element resembles the complex transadmittance element by design (see Figure 6).

$$\frac{d\hat{H}}{dt} = \frac{i}{\hbar}\left[\hat{H}, \hat{H}\right] = 0 \qquad \frac{d\langle V|I\rangle}{dt} = -\frac{d\langle I|V\rangle}{dt} = 0$$
$$\langle\psi|\psi\rangle = 1 \qquad \frac{C\hbar}{2}\langle V_\psi|V_\psi\rangle = E$$
$$\langle H\rangle = E \qquad \langle V_\psi|I_\psi\rangle = -iP$$

Conservation Laws Conservation Laws

Figure 7: A summary of how the conservation laws in quantum mechanics map to conservation laws in our analog circuit emulations of such dynamical systems.

4 Emulation of Quantum Dynamics in Two-State Systems and Conservation Laws

In this section, we provide theory, measurements, and simulations of how probability and energy conservation in quantum Hamiltonians maps to Planck capacitor energy conservation and conservation of reactive power flow in our classic Hamiltonians that emulate it, the summary of which can be seen from Figure 7 (Sarpeshkar, 2019, 2019b, 2019c, 2020; Feynman et al., 2011).

It is important to note that quantum mechanics generalizes the key notion of conserved reactive power in classical passive inductor-and-capacitor circuits to significantly more symmetric and general notions of conserved reactive power in our active analog circuits that emulate its Hamiltonians. From a circuit standpoint, each of the four parts that we have discussed requires two real-valued voltages and two real-valued currents to operate and cannot be instantiated with one real-valued voltage and one real-valued current as in passive classical LC (or lossy LCR) circuits. We now discuss the mapping of conservation laws in more detail.

4.1 Conservation of Probability Maps to Conservation of Planck Capacitor Energy. First, we recall the mapping of the complex quantum Hamiltonian to the purely real-valued circuit system:

$$i\hbar\frac{d}{dt}|\psi\rangle = H|\psi\rangle$$
$$\Downarrow$$
$$\hbar\frac{d}{dt}\begin{bmatrix}\psi^R\\ \psi^I\end{bmatrix} = \begin{bmatrix}H^I & H^R\\ -H^R & H^I\end{bmatrix}\begin{bmatrix}\psi^R\\ \psi^I\end{bmatrix}.$$

We want to show that $\langle\psi|\psi\rangle = 1$ corresponds exactly to $\frac{1}{2}C_\hbar\langle V|V\rangle = E$, the sum of the capacitor energies of the circuit system:

$$\begin{aligned}\frac{1}{2}C_\hbar\langle V|V\rangle &= \frac{1}{2}C_\hbar\left(\langle V^R| - i\langle V^I|\right)\left(|V^R\rangle + i|V^I\rangle\right)\\ &= \frac{1}{2}C_\hbar\left[\left(\langle V^R|V^R\rangle + \langle V^I|V^I\rangle\right) + i\left(\langle V^R|V^I\rangle - \langle V^I|V^R\rangle\right)\right]\\ &= \frac{1}{2}C_\hbar\sum_{i=1}^{N}(V_i^R)^2 + (V_i^I)^2\\ &= E.\end{aligned}$$

We note that we must maintain the complex number structure of the inner product, as we lose the cross-terms when simply using row/column vectors for the real/imaginary parts. To show that the capacitor energy remains constant, we now show that the time derivative is zero:

$$\begin{aligned}\frac{\mathrm{d}}{\mathrm{d}t}\left[\frac{1}{2}C_\hbar\langle V|V\rangle\right] &= \frac{1}{2}C_\hbar\frac{\mathrm{d}}{\mathrm{d}t}\left[\left(\langle V^R| - i\langle V^I|\right)\right]\left(|V^R\rangle + i|V^I\rangle\right)\\ &\quad + \frac{1}{2}C_\hbar\left(\langle V^R| - i\langle V^I|\right)\frac{\mathrm{d}}{\mathrm{d}t}\left[\left(|V^R\rangle + i|V^I\rangle\right)\right]\\ &= \frac{1}{2}\left(\langle V^R| - i\langle V^I|\right)G^T\left(|V^R\rangle + i|V^I\rangle\right)\\ &\quad + \frac{1}{2}\left(\langle V^R| - i\langle V^I|\right)G\left(|V^R\rangle + i|V^I\rangle\right)\\ &= \frac{1}{2}\langle V|\left(G^T + G\right)|V\rangle\\ &= 0.\end{aligned}$$

Figure 8 shows that in two-state systems such as those in Figure 12, as probability ideally shuttles back and forth between two states undergoing constant transitions (a resonant control input may be always on to enable such transitions), capacitive energy shuttles back and forth between Planck capacitors corresponding to each state. However, the total energy is always conserved corresponding to the fact that total probability is always conserved in the unitary evolution. These are ideal, lossless results performed via circuit simulation software (Cadence).

Actual measured capacitor energies from our chip in the Figure 9 are similar but are not as ideal due to circuit mismatch and inevitable loss (seen in the two-state dynamics of Figure 12 as well).

4.2 Conservation of Energy Maps to Conservation of Planck-Capacitor Power Flows. Similarly, we may show that $\langle\psi|H|\psi\rangle = E$ corresponds exactly to the reactive power flows in the circuit $\langle V|I\rangle = -\langle I|V\rangle = -iP$.

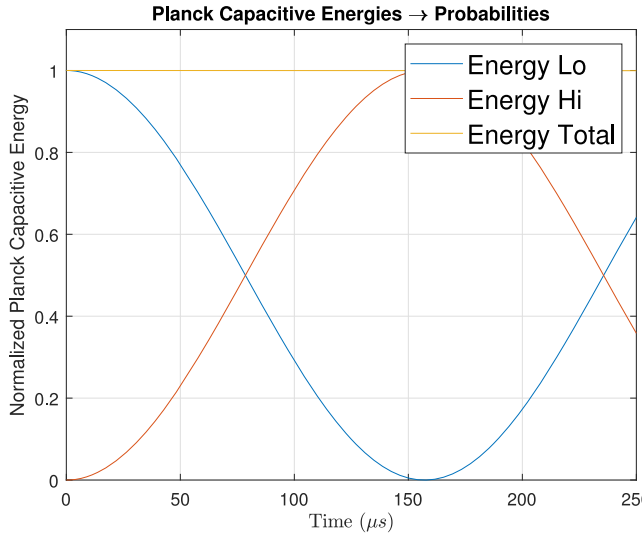

Figure 8: A simulation of how the Planck capacitive energies oscillate back and forth between the two states, as the "probability" flows from one side to the other.

Now,

$$\begin{aligned}
\langle V|I\rangle &= \left(\langle V^R| - i\langle V^I|\right)\left(|I^R\rangle + i|I^I\rangle\right) \\
&= \left(\langle V^R|I^R\rangle + \langle V^I|I^I\rangle\right) + i\left(\langle V^R|I^I\rangle - \langle V^I|I^R\rangle\right) \\
&= i\left(\langle V^R|I^I\rangle - \langle V^I|I^R\rangle\right) \\
\implies \langle I|V\rangle &= i\left(\langle V^I|I^R\rangle - \langle V^R|I^I\rangle\right) \\
&= -\langle V|I\rangle.
\end{aligned}$$

Note that the $\langle V^R|I^R\rangle + \langle V^I|I^I\rangle$ term disappears since it is simply $\frac{C_\hbar}{2}\frac{\mathrm{d}}{\mathrm{d}t}\left(\langle V^R|V^R\rangle + \langle V^I|V^I\rangle\right)$, which from our previous discussion is exactly zero. The $\langle V^I|I^R\rangle - \langle V^R|I^I\rangle$ term is identified with the reactive power.

To show that the reactive power flows remain constant, we now show that the time derivative is zero:

$$\begin{aligned}
\frac{\mathrm{d}}{\mathrm{d}t}\langle V|I\rangle = &\frac{\mathrm{d}}{\mathrm{d}t}\left[\left(\langle V^R| - i\langle V^I|\right)\right]\left(|I^R\rangle + i|I^I\rangle\right) \\
&+ \left(\langle V^R| - i\langle V^I|\right)\frac{\mathrm{d}}{\mathrm{d}t}\left[\left(|I^R\rangle + i|I^I\rangle\right)\right]
\end{aligned}$$

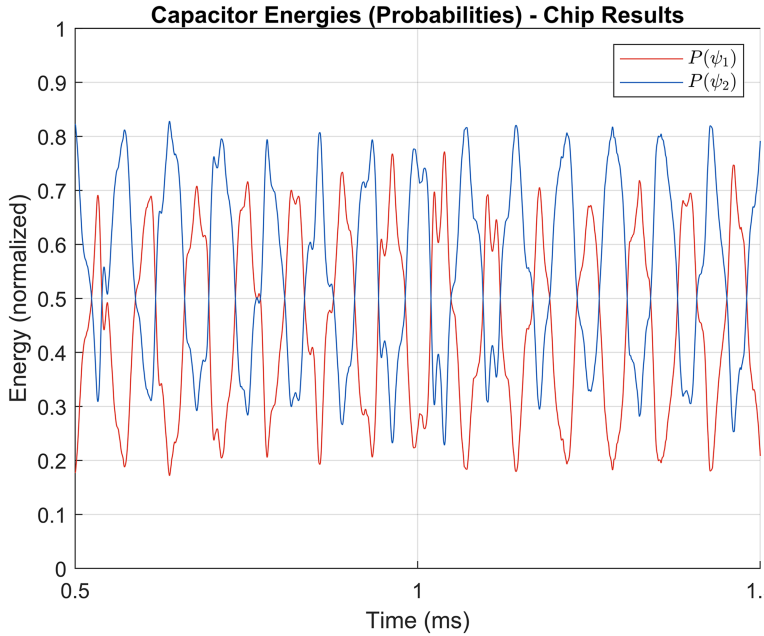

Figure 9: Experimental results of the Planck capacitive energies, which are not as ideal due to circuit mismatches (finite Q and loss as in actual quantum systems as well).

$$
\begin{aligned}
&= \left[\left(\langle V^R| - i\langle V^I| \right) \frac{G^T}{C_\hbar} \right] \left[G \left(|V^R\rangle + i|V^I\rangle \right) \right] \\
&\quad + \left[\left(\langle V^R| - i\langle V^I| \right) \right] \left[\frac{G^2}{C_\hbar} \left(|V^R\rangle + i|V^I\rangle \right) \right] \\
&= \frac{1}{C_\hbar} \left(\langle V^R| - i\langle V^I| \right) \left(G^T G + G^2 \right) \left(|V^R\rangle + i|V^I\rangle \right) \\
&= 0.
\end{aligned}
$$

An equivalent derivation (of both cases) is based on Ehrenfest's well-known theorem for the average rate of change of an operator (Feynman et al., 2011), summarized in Figure 7 (Sarpeshkar, 2019a, 2019b, 2019c, 2020; Feynman et al., 2011), which this derivation has stepped through in more detail.

Energy conservation in quantum Hamiltonians maps to reactive Planck capacitor power flow conservation in our classical Hamiltonian emulations. As energy oscillates back and forth in a conservative fashion between two states in a quantum system, reactive power oscillates back and forth

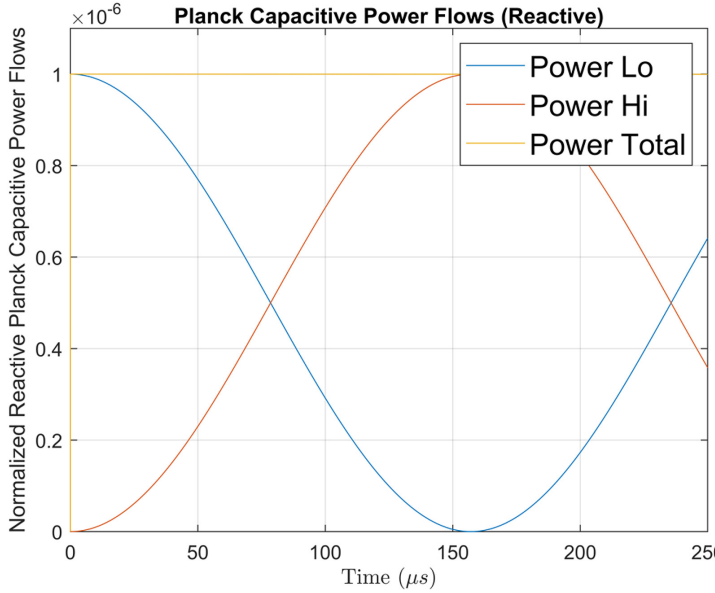

Figure 10: Simulation of Planck capacitor reactive power flows, which sum to a constant value.

between the corresponding two states in the corresponding classical two-state emulation. Ideal circuit simulations and chip results are shown in Figures 10 and 11.

5 Emulation of Controlled Quantum Dynamics in Two-State Systems

The circuit to classically create and emulate the dynamics of a quantum two-state system with a $\mu_E E$ control input and $V_{\psi i}$ state probability-amplitude outputs is shown in Figure 12, representing those in NMR or optical systems (Nielsen & Chuang, 2010; Feynman et al., 2011). Such a two-state system may correspond to one with a control input like a dynamic B_x or B_y field architecting state transitions between two spin states of an electron in a strong nonvarying B_z field. The energy levels of the two states are proportionally represented by the values of the two quantum admittances G_{E_1} and G_{E_2}, and the probability amplitudes of the corresponding states are represented by the voltages on the $C_\hbar$ Planck capacitors as shown. The quantum transadmittance mixer elements use dynamic control inputs proportional to $e^{-i\omega t}$ or $e^{+i\omega t}$ explicitly instantiated via classical sine and cosine waveforms. They architect resonant complex up-mixing or down-mixing state transitions between the energy levels separated in energy by $E_2 - E_1 = \hbar\omega$ or, equivalently, $G_{E_2} - G_{E_1} = C_\hbar\omega$. The layout for an actual classical analog

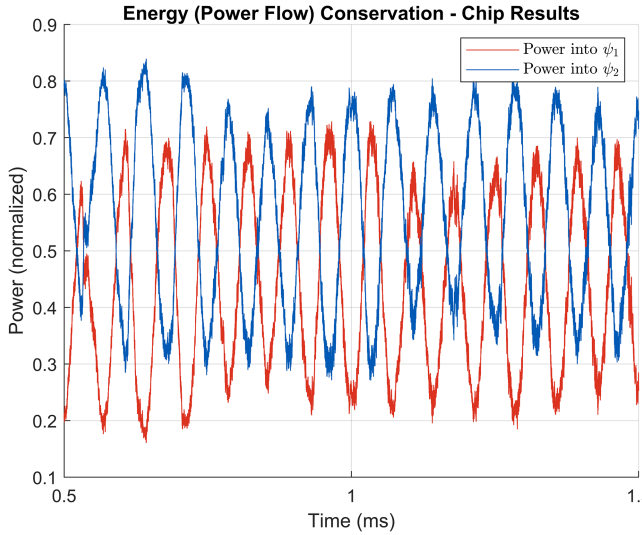

Figure 11: Experimental results of the Planck capacitor reactive power flows, which again are not as ideal due to circuit mismatch losses.

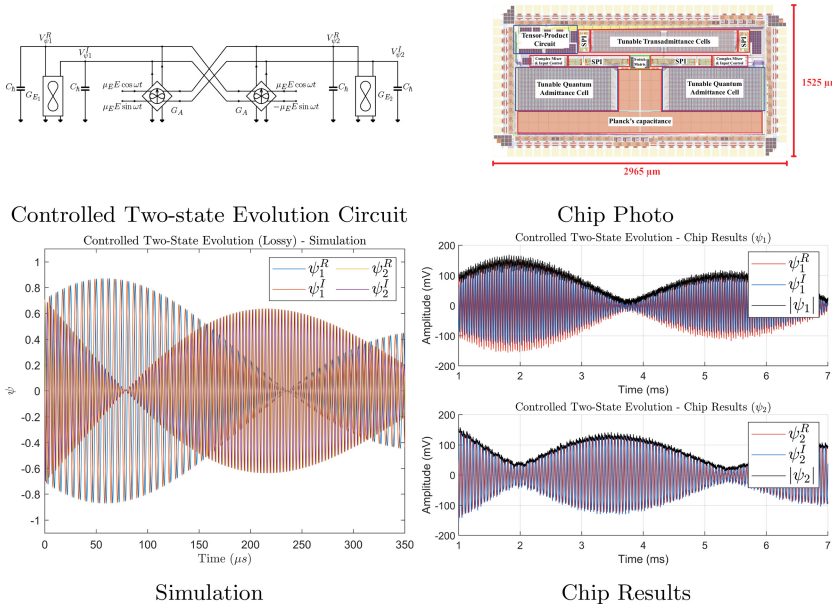

Figure 12: A demonstration of a lossy controlled two-state system in both simulation and using fabricated chips.

circuit instantiation built on an integrated circuit is shown on the right in Figure 12 with the die photo.

The oscillations of all voltage probability amplitudes in the circuit of row 1 in response to a persistent control input are shown. There is a slow oscillation of probability amplitude from one state to another and back as in a Rabi oscillation. The Matlab simulation of the dynamics that incorporates a small amount of loss is shown on the left. Such loss is due to dissipation and incoherence that are always present in experimental quantum or classical analog systems that must inevitably couple with their environments or have nonidealities such that they are not perfectly energy conserving and Hamiltonian. The loss is easily incorporated as a small conductance in parallel with the $C_\hbar$ capacitors, corresponding to finite d.c. gain in circuit transconductances as described in Sarpeshkar (2019a, 2019b, 2019c, 2020), or, equivalently, G_E has a small imaginary component. The dynamics of the actual experimental analog circuit are seen to be very similar. However, due to circuit offsets, nonlinearities, and the propensity for slight instability, all common in high-Q active systems, it is hard to always get perfectly zero amplitudes in all waveforms simultaneously. As in prior reported quantum (Arute et al., 2019), neuromorphic (Pedroni, Deiss, Mysore, & Cauwenberghs, 2020), and classical (Sarpeshkar, 2010) systems, future implementations with well-known digital calibration techniques and machine learning can help make such practical realizations more perfectly ideal.

6 NMR and Josephson Junction Emulation with Two-State Circuits

Using these circuit building blocks, Figure 12 shows how to create and emulate an important coherent quantum dynamical system: a two-state system with a controlled input that can architect state transitions analogous to single qubit gates in quantum computation. Here, our parts enable state transitions between two states at different energy levels with simulations and measured data from our chip in good agreement. Two-state systems are important in nuclear magnetic resonance (NMR) where pulses of finite duration (e.g., 90° or 180° pulses) architect transitions in two-state systems in a controlled fashion. Figure 13 shows that controlled pulses of finite duration architect similar state transitions with our building blocks in our chip and in circuit simulations. Measured data in Figure 13 also show that reactive power flows in the Planck capacitors in our two-state system, which correspond to probability currents from the conservation theorems of Figure 7, successfully emulate currents in Josephson junctions. The latter currents are directly proportional to these probability currents (Feynman et al., 2011) ideally or to normalized probability currents if there is loss.

In Figure 13, both circuit simulations (left) and actual chip results (right) show that pulsatile control inputs of finite duration (e.g., an 180° pulse) can cause state transitions wherein energy is transferred from one state to another or vice versa.

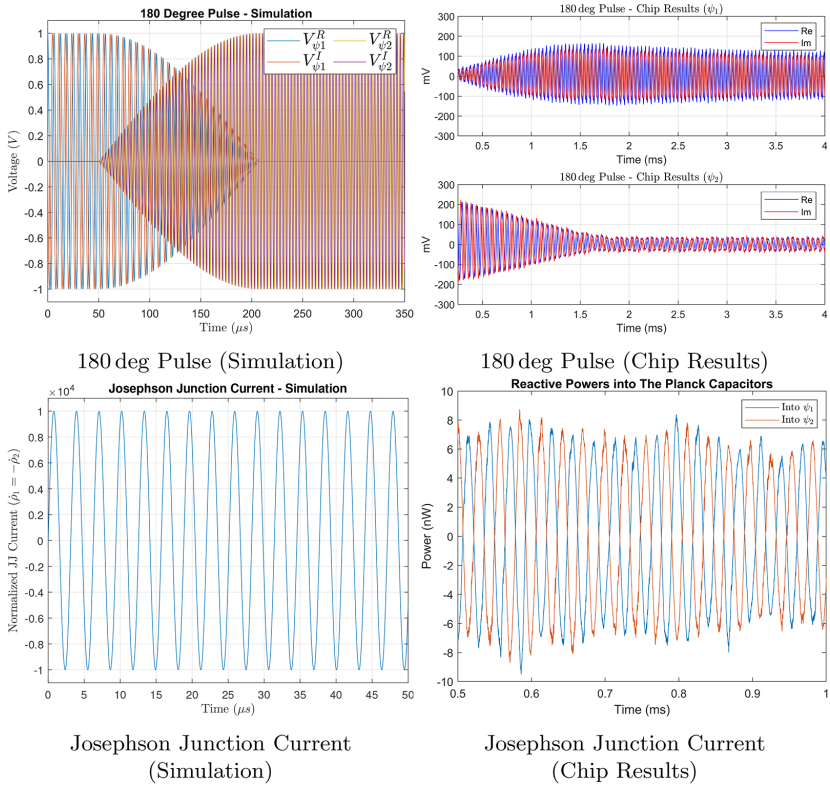

Figure 13: Demonstration of a 180° pulse (top row) and emulation of a Josephson junction (bottom row).

Josephson junction currents can be modeled to correspond to probability current flow in a two-state system with the energy difference between the two states imposed by the voltage across the junction and the current proportional to the strength of the coupling between the two sides of the junction (Feynman et al., 2011). Thus, in our two-state emulations, in which probability is represented by Planck capacitor energies corresponding to each state, probability current flows in computer simulations in Figure 13 (left) and experimentally measured reactive power flow into the Planck capacitors on our chip in Figure 13 (right) show similar sinusoidal oscillations. The oscillations arise as probability current flows back and forth across a junction or two-state system with symmetric and constant coupling between the two states. The reactive power flows were measured by determining voltage-current or $C_\hbar V \cdot \mathrm{d}V/\mathrm{d}t$ products on the Planck capacitors on our chip. A larger energy difference between the two states corresponding

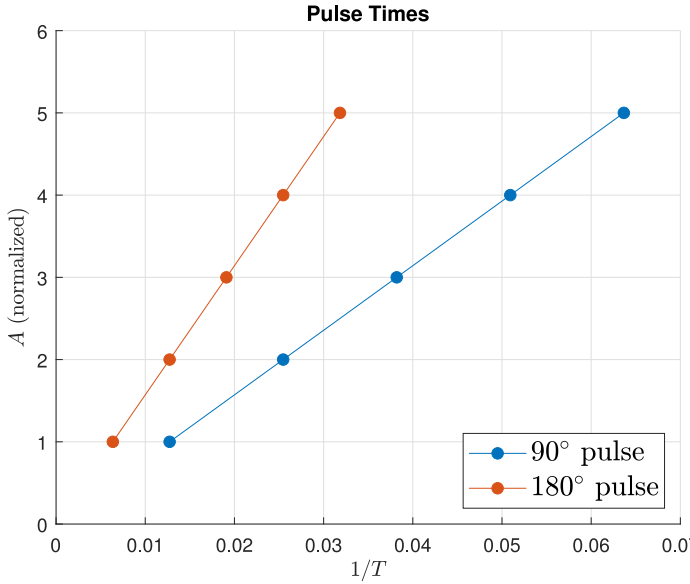

Figure 14: An illustration of how the required pulse times scale with the strength of the pulse (A).

to a greater voltage difference across the junction leads to higher-frequency sinusoidal oscillations in actual junctions as well as in our emulations.

It is worth noting here that the Kuramoto model (Kuramoto, 1984) for nonlinear oscillator coupling has been used to model Josephson junctions as well as coupling among fireflies and neurons. Recent work (Budzinski et al., 2021) has shown that the use of complex-number-like quadrature oscillations enables nonlinear coupling to be more easily understood in a more linear framework. Our complementary work described here and in Sarpeshkar (2019a, 2019b, 2019c, 2020) is in accord with such recent work.

Figure 14 shows simulations of the two-state circuit corresponding to Figure 12. In these simulations, we can vary the pulse width of the control input that architects state transitions, T, as we change its signal strength A. We observe that as in actual NMR systems, a strong pulse (large A) that integrates for a short time is as effective at causing a transition as a weak pulse (small A) that integrates for a shorter time. Thus, A is proportional to $1/T$. The 90° pulse, which architects state transitions in which both states have equal probability amplitude, as expected has a slope that is half that of the 180° pulse, which architects state transitions wherein energy flips completely from one state to another. The data points were obtained from circuit simulations of the circuit shown in Figure 12. The lines are merely straight-line fits to such simulation data.

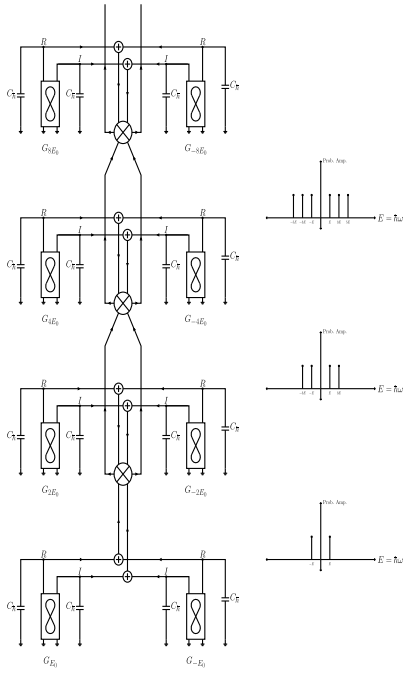

Tensor Product Architecture

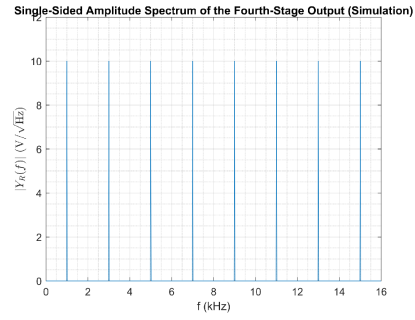

Spectrum of Simulation

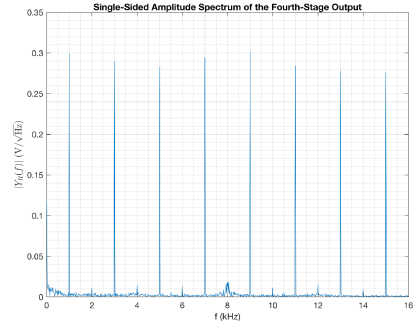

Spectrum of Chip Results

Figure 15: Left: An architecture for the tensor product as a series of cascading complex multiplications. Right: We compare the theoretical and experimental spectra of a simple tensor product input.

7 A Classical Tensor-Product Architecture for Efficient Emulation of a Superposition of Quantum States

One important benefit of quantum systems is that they can simultaneously be in a superposition of many states even if we cannot access all of them simultaneously. Figure 15 shows a classical tensor-product architecture that efficiently creates superpositions of an exponential number of states with a linear number of our complex mixer circuits even though they are not all simultaneously accessible (Sarpeshkar, 2019a). More formally, the classical circuit shown in Figure 15 emulates a superposition of 2^n quantum states as the spectrum of two real and imaginary output classical signals. The circuit hardware resources are proportional to $n + 1$, as can be easily seen from Figure 15. These comprise n emulated quantum two-state systems, indexed by $k = 0, 1, 2, 3, \ldots, n$, with each two-state system with two emulated quantum admittance circuits with quantum admittance values of $+iE_0 2^k$ and $-iE_0 2^k$. The complex outputs of each of the two admittances at

each level are summed to architect a superposition of two states within each two-state system. These are then mixed, in a complex mixer, with analogous superposed signals from the corresponding two-state system with index $k+1$ such that the resulting mixed signal creates a new signal that represents a superposition of 2^{k+1} states at exponentially many distinguishable frequency locations. We then reinitiate this process in a recursive fashion such that recursive process initiates at $k=0$ and terminates at $k=n-1$. The final output signals will then represent a superposition of 2^n quantum states. For maximum superposition capability, the probability of the two states of each of the emulated two-state quantum systems of any index k is $^1/_2$. In this case, the superposition of all 2^n quantum states in the final output signal has an equally balanced probability among all states, as for well-known Hadamard-transformed bases in quantum computing. Figure 15 also shows that circuit simulations and measured data from our silicon chip show good agreement.

Our silicon integrated-circuit chip was built in a 0.18 μm process using transconductor-capacitor circuits with our four circuit parts to instantiate the architecture of Figure 15. The circuits are similar to those described in depth in Sarpeshkar (2019a, 2019b, 2019c, 2020).

The analog-circuit parts enable unitary dynamics as we have shown in mathematics and discussions pertinent to Figures 1 to 14. They can be used to compose any $2N \times 2N$ matrix Hamiltonian with state maintained on Planck capacitors, diagonal terms implemented with quantum admittance parts, and off-diagonal terms implemented with controlled or constitutive quantum transadmittance parts. Tensor-product emulations like that of Figure 15, which are also built with these parts, provide us with a foundation for emulating more complex transforms (e.g., the QFT), as we show below. In our emulations, nondestructive coherent measurement and readout is possible, which can be useful in quantum-inspired systems that do not need to have probabilistic readout, as in many quantum systems. However, it is also possible to emulate probabilistic readout with amplified thermal noise and Poisson processes as described in Kim et al. (2018) to emulate quantum measurement. Finally, by converting differential to difference equations that approximate them, distributed systems like Schrodinger's equation can be built using these parts as well (Sarpeshkar, 2019a, 2019b, 2019c, 2020). While we can emulate many quantum systems, we focus on the important example of the QFT below. The maximally superposed states of Figure 15 are particularly important in the QFT.

8 The Quantum Fourier Transform

8.1 Architecture. Figure 16 shows an architecture for emulating the QFT that builds on the foundational tensor-product architecture of Figure 15. Suppose each of the quantum admittances in the tensor-product architecture of Figure 4 has its quantum admittance value synchronously

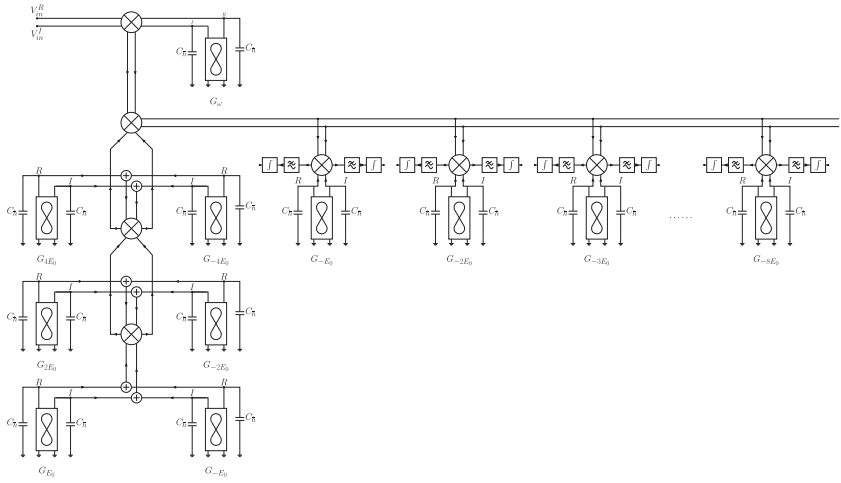

Figure 16: An architecture for the QFT. In the lower left, we generate the necessary carrier signals, in the upper left we take an input signal, and along the right we read out the voltages corresponding to each value in the QFT of the input.

modulated at an angular frequency much slower than $G_2^k E_0/C_\hbar$ and proportional to it, such that there is slow phase modulation at all $G_2^k E_0/C_\hbar$ carrier frequencies. Then, when the smallest quantum admittances at the bottom rung of the hierarchy architect a full $\pm\pi$ phase change, the quantum admittances at the next rung of the hierarchy will architect a full $\pm 2\pi$ phase change, the quantum admittances at the rung above that will architect a full $\pm 4\pi$ phase change, and so on. The phase changes from any rung of the hierarchy will affect all rungs above it and add to them. The cascade of mixing operations in Figure 15 will then effectively scan through every single column of a QFT phase-modulation matrix within one time period of the slowest modulation rung (the bottom rung), modulating the phases of the eigenfrequencies/carrier frequencies of Figure 15 according to the columns of a QFT matrix as modulation time proceeds.

If, during this time, we weight the final R and I outputs in Figure 15 by values corresponding to the complex column input vector of the QFT, a row scan of the input column vector that is synchronous with the QFT matrix column scan results. Figure 16 shows the weighting input admittances, G_ω, and inputs necessary to perform the latter operations. Note that continuous analog synchrony is maintained throughout the process such that a discrete clock to maintain synchrony is not necessary. However, when one time period of the slowest modulation rung is complete, every carrier frequency will have acquired a net phase, which can be read out via classical

demodulation of an array of mixers tuned to the eigenfrequencies as shown in Figure 16, and with the integration duration for demodulation being the latter time period. The demodulators can be multiplexed to save hardware resources, but equivalent costs then manifest in time rather than in hardware resources, so we have shown them in parallel in Figure 16, and as implemented in our current chips.

Our nondestructive classical readout scales like 2^n (analogous to the probabilistic readout of 2^n in quantum systems), and our scanning classical read-in scales like 2^n, the best that can possibly be done to read in 2^n input values of classical information in any architecture, conceptually or physically, quantum or classical. However, as Figure 16 illustrates, the processing hardware for our emulated QFT is inspired by and emulates the tensor-product and superposition advantages of the actual QFT and scales like n with respect to the use of hardware resources. If we read out the output with just a global property such that full readout is not necessary or if the classical input column information is read in only once during initialization of a state, the costs due to classical read-in and readout can be minimized with regard to the costs of the QFT. For example, we can continue to perform many unitary phase-change operations in sequence (Gilyén, Su, Low, & Wiebe, 2019) with an eventual final readout that reflects a global property. Later, we show that the ideal QFT as computed via Matlab simulations is in accord with that of experimental measurements of the QFT implemented on our chip.

8.2 Measurements. In the QFT instantiation of Figure 15, based on that figure's tensor-product architecture, we employ three complex mixers to multiply four analog inputs together, each of the form $x_k(t) = e^{-i2^{k-1}\omega_c t} + e^{i2^{k-1}\omega_c t}$ for $k \in \{1, \ldots, 4\}$, to generate the tensor-product signal $m(t) = \sum_{k=-7}^{7} e^{-ik\omega_c t}$ for odd k. Hence, using such a form of $x_k(t)$ makes inaccessible the computation of the quantum Fourier transform coefficients for even k's. Nevertheless, a simple modification to the input signals $x_k(t)$ makes it possible to generate a tensor product of the form $m(t) = \sum_{k=-N}^{N} e^{-ik\omega_c t}$ for all integers $k \in \{-N, \ldots, N\}$. The trick is to add a constant term into each $x_k(t)$ while choosing appropriate frequencies for its complex sinusoids. For example, we can make $x_1(t) = 1 + e^{-i\omega_c t} + e^{i\omega_c t}$, $x_2(t) = 1 + e^{-i3\omega_c t} + e^{i3\omega_c t}$, $x_3(t) = 1 + e^{-i9\omega_c t} + e^{i9\omega_c t}$, and $x_4(t) = 1 + e^{-i27\omega_c t} + e^{i27\omega_c t}$. Multiplying these input signals together will give us $m(t) = \sum_{k=-40}^{40} e^{ik\omega_c t}$. The result in Figures 17 and 18 shows the QFT of an input sequence α_j which consists of spectral lines at all $k \in \{-7, \ldots, 7\}$.

Our chip results are in reasonably good agreement with theory, just as for another example shown in Figure 19. In the example shown in Figure 19, there is better agreement between the real portions of all signals, which are relatively strong and nonzero than the imaginary components, which are weak and zero. Nevertheless, our first-time silicon proves the experimental

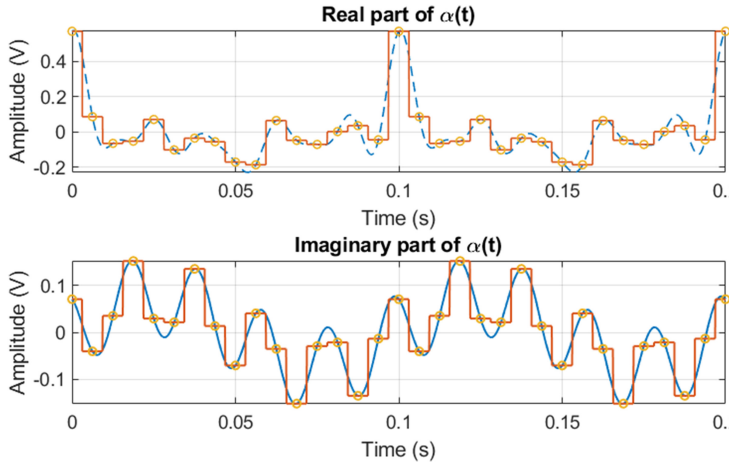

Figure 17: Demonstration of generating the real and imaginary input signals for the QFT (continuous signal superimposed on the ideal rectangular pulse sequences).

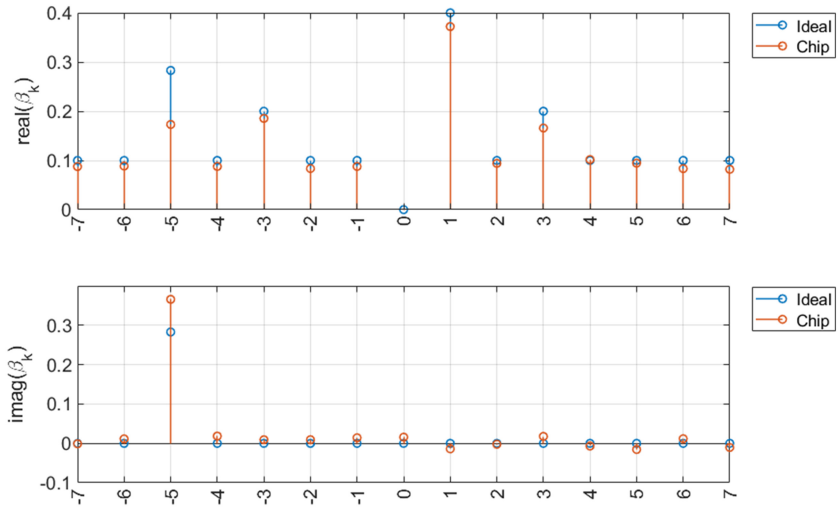

Figure 18: Demonstration of the QFT readout.

feasibility of the architecture of the quantum-inspired architecture of Figure 15 from a fundamental and scientific point of view. Standard digital calibration and machine learning improvements in analog integrated

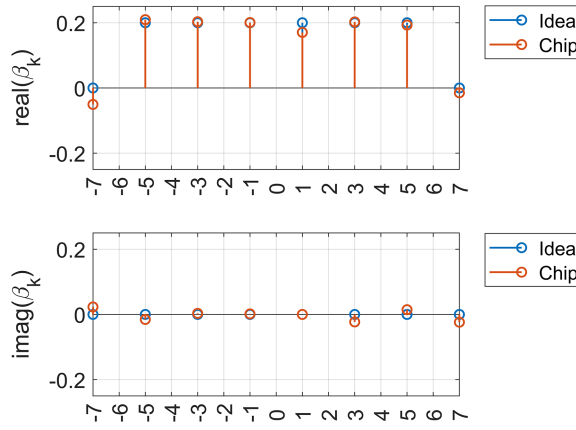

Figure 19: Another demonstration of a QFT readout.

circuit engineering can architect significant improvements in the future (Sarpeshkar, 2010).

It is worth noting that prior work has proposed using a cascade of mixers to solve the subset sum problem (SSP; Traversa, Ramella, Bonani, & Di Ventra, 2015). It also exploits the exponential growth in spectral content that arises from mixing of an underlying set of inputs. However, as it attempts to solve a different problem from ours, its circuit and algorithmic architecture is different from our tensor-product circuit architecture of Figure 15. Its architecture is also different from the algorithm and architecture needed for the QFT in Figure 16. We now outline these differences since they shed further insight into our implementation.

Cascades of mixers are well known in RF circuits for implementing single-stage or multistage super-heterodyne RF receivers via summation and differencing of spectral lines (Sarpeshkar, 2010) to generate new harmonic content. We exploit this feature in our tensor-product architecture such that $O(2^n)$ spectral lines with the right phase and magnitude are generated via $O(n)$ quantum-transadmittance-emulating mixers and quantum-admittance-emulating oscillators to faithfully emulate quantum superposition and dynamics. These lines must have no overlap (Sarpeshkar 2019a, 2019b, 2019c, 2020) or they cannot coherently represent a superposition of all quantum states in the spectral domain in general, without having them degenerate into one another. In contrast, the SSP exploits the fact that the harmonic amplitude of input-subset spectral lines can sum in various ways to create the same degenerative output spectral output line in many convolutionally different ways; thus, the harmonic amplitude of an output spectral line is nonzero if there is a solution and larger if there are many subset sums that all sum to the same output. As in our scheme or in quantum

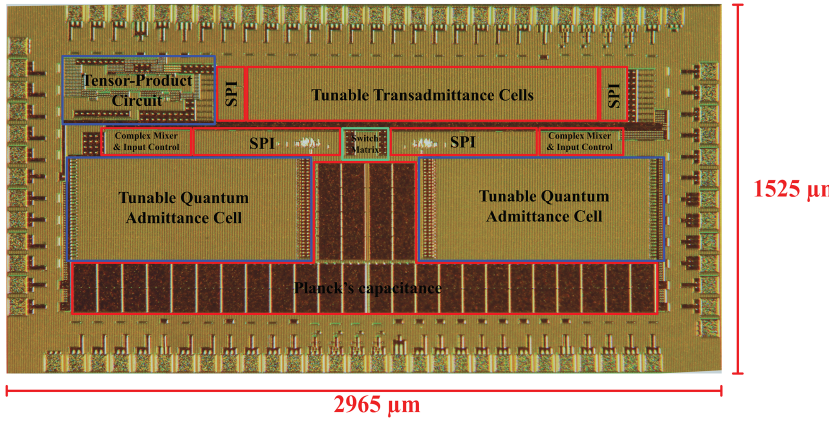

Figure 20: The die photo of our fabricated 0.18 μm chip.

measurement, the specific output readout requires demodulation, as is also implemented in Traversa et al. (2015). Neither scheme solves an NP-complete problem unless infinite-precision analog variables with no noise exist (impossible by the quantum fluctuation-dissipation theorem at any finite temperature; Sarpeshkar, 2019a, 2019b, 2019c) or, alternatively, if Heisenberg time-frequency uncertainty trade-offs are ignored (also impossible). Nevertheless, finite-precision collective analog computation, with real or complex numbers, can be powerful as we have outlined here and elsewhere (Sarpeshkar, 1998, 2002, 2010) and as also outlined in (Traversa et al., 2015).

Finally, our QFT also requires a coherent slow modulation on the phase of all of these spectral 2^n spectral lines and leverages the very same tensor-product architecture to architect it. Therefore, it creates exponentially generated phase content that, for an arbitrary 2^n QFT inputs synchronously scanned with such phase, yields the correct output phase, available for readout, on all 2^n QFT outputs via demodulation or on the synchronously superposed time-domain, real-valued output pair. The SSP, with its n inputs, does not have to, and does not, have slow phase modulation on its inputs. Therefore, it does not implement all of these 2^n matrix multiples in a parallel and coherent fashion with n resources.

9 Details of Experimental Chip Measurements

The die photo for our fabricated 0.18 μm chip is shown in Figure 20. This chip was used to instantiate all of our digitally programmable analog circuits and tested with the experimental setup described. In sequence, we

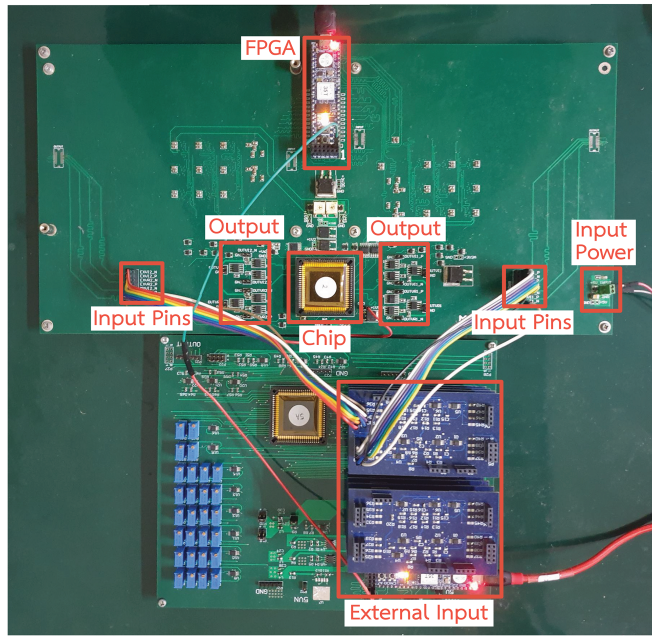

Figure 21: The two-state system test setup.

describe our measurements for the various analog circuits and systems reported in this article.

Figure 21 shows a measurement system to verify the functionality of the on-chip quantum two-state system. The system can be configured as either a quantum transadmittance (requiring no external inputs) or a quantum transadmittance mixer (requiring external inputs through the on-chip complex mixers). Programming the chip into any one of the two settings is performed via an on-board field programmable gate array (Cmod A7, Artix-7 FPGA from Digilent Inc.). For the quantum transadmittance setting, we program the two on-chip tunable quantum admittance cells to oscillate at two slightly different frequencies and couple them together via the on-chip tunable coupling admittance cells, whose coupling strengths can also be controlled by the FPGA. For the quantum transadmittance mixer setting, which requires external inputs, we have digital-to-analog converter boards (two columns of four vertically stacked DAC boards, labeled "External Input" in Figure 21) to convert digital waveforms—generated by the FPGA with the direct digital synthesis technique—into two analog complex input signals into the chip. The output of the chip is then read out by an 8-bit USB mixed-signal oscilloscope (PicoScope 3000 Series, Pico Technology) into a computer for further processing by Matlab.

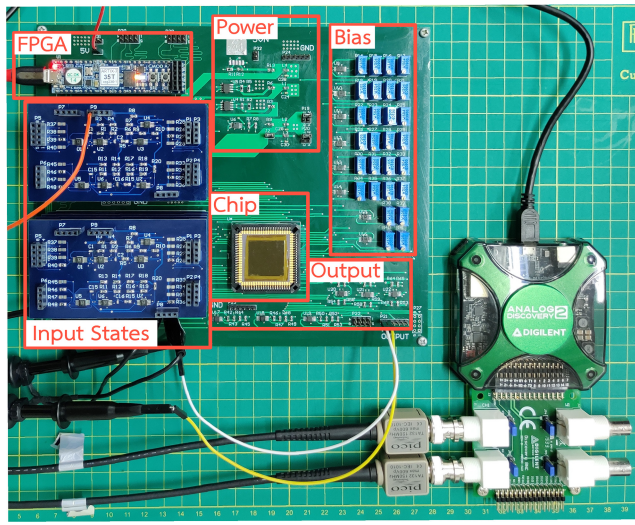

Figure 22: The tensor product test setup.

Figure 22 shows the measurement system to verify the functionality of the on-chip tensor-product circuit. The chip, emulating a four-stage tensor product circuit, consists of several adders and three complex mixers to generate a tensor product from eight complex analog inputs, which are generated via digital synthesis by an on-board FPGA (Cmod A7, Artix-7 FPGA from Digilent Inc.) and eight DAC boards. The frequency of each complex analog input can be programmed to range from 10 Hz to 100 kHz in steps of 0.025 Hz. The output of the chip (the tensor product) is then buffered by on-board circuits before being read out into a computer by a USB mixed-signal oscilloscope (Analog Discovery 2, Digilent Inc.).

Figure 23 shows the QFT circuit based on the on-chip tensor product circuit. Provided the input sequence α_j, $j \in \{0, \ldots, N-1\}$ where N is the number of points, the QFT circuit is to perform a discrete Fourier transform operation $\beta_k = \frac{1}{\sqrt{N}} \sum_{j=0}^{N-1} \alpha_j e^{i\frac{2\pi}{N}kj}$. The QFT circuit makes use of the on-chip, tensor-product circuit to construct a superimposed state to compute each β_k in a quantum Fourier transform manner. First, from the input sequence α_j, the QFT generates an interpolated analog signal $\alpha(t)$ of the period T—by the input interpolator consisting of two vertically stacked DAC boards and an FPGA—such $\alpha\left(t = \frac{j}{N}T\right) = \alpha_j$. It then generates a tensor product $m(t) = \sum_{k=-N}^{N} e^{i\left(\omega_c + \frac{2\pi}{T}\right)kt}$—via the tensor-product generator consisting of an FPGA, eight DAC boards, and an on-chip tensor-product circuit (chip 1)—where ω_c is the fundamental carrier frequency and $2\pi/T$ the frequency offset from ω_c. The interpolated input signal $\alpha(t)$ is then multiplied to the tensor product

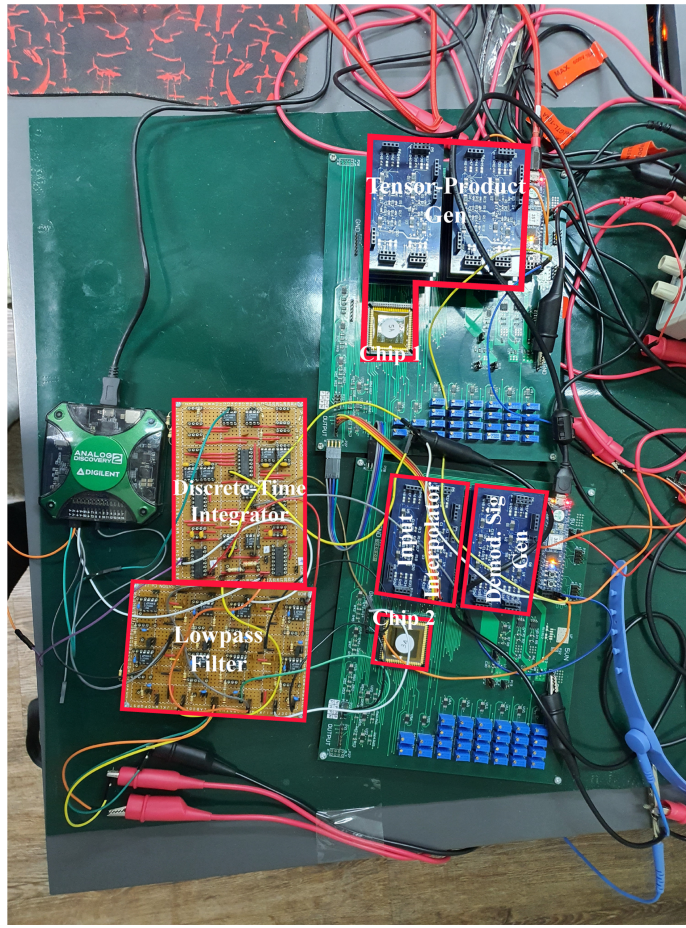

Figure 23: The quantum Fourier transform test setup.

$m(t)$ by an on-chip complex mixer (within chip 2) to create a complex signal of the form $y(t) = \alpha(t) \cdot m(t) = \sum_{k=-N}^{N} \left(\alpha(t) e^{i\frac{2\pi}{T}kt}\right) e^{ik\omega_c t}$.

Note that the spectrum of $y(t)$ now consists of amplitude-and-phase-modulated spectral lines centered at multiples of ω_c. To compute the Fourier transform coefficient for each k, we generate a demodulating signal of the form $d(t) = e^{-ik\omega_c t}$ via the demodulating signal generator (consisting of two DAC boards), multiply it to $y(t)$—by another complex mixer within chip 2—and then low-pass-filter the result with a fourth-order Butterworth filter with a -3 dB cutoff frequency at 400 Hz to get rid of unwanted harmonics, thus providing the output of the form $\alpha(t) e^{i\frac{2\pi}{T}kt}$. The discrete-time integrator

then samples this signal at the time instants $t_j = \frac{j}{N}T$, $j \in \{0, \ldots, N-1\}$ and sums all of the N samples to provide the output of the form $\sum_{j=0}^{N-1} \alpha_j e^{i\frac{2\pi}{N}kj}$. The output of the discrete-time integrator is then read into a computer via a USB oscilloscope and is normalized by a factor of $1/\sqrt{N}$ to provide the coefficient β_k. The process is then repeated in time to obtain the coefficients for all k's.

10 Discussion

Coherent computation requires careful maintenance of phase relationships among classical analog real variables just as it does among quantum analog complex variables as well. Thus, as in Arute et al. (2019) and Pedroni et al. (2020), machine learning and digital calibration of analog mismatch and error are useful, as is well known in the field of analog and biological circuit engineering, for example, in low-power cochlear-implant processors for the deaf (Sarpeshkar, 2010) or in digitally programmable cytomorphic processors for biological cell simulations (Woo, Kim, & Sarpeshkar, 2018; Teo & Sarpeshkar, 2020). Here, we have focused on the more fundamental science of how to formulate and emulate quantum systems with good scaling with respect to hardware costs without which such engineering would not even be feasible. Our integrated-circuit hardware implementation in a 0.18 μm silicon process with classical operation at room temperature proves feasibility, experimentally. Our mathematical results with associated circuit topologies prove how unitary dynamics for arbitrary N arise, theoretically. In our current embodiments, our circuits are limited in operating time to the slowest $E_0/\hbar$ frequency of oscillation of the smallest E_0 quantum admittance and, for some applications like the QFT, require a fastest oscillation frequency of $(E_0 2^n)/\hbar$, corresponding to the largest quantum admittance. Fortunately, in modern silicon processes, where more than 10 GHz operation is easily possible, real-time operation with $n \approx 40$ may enable many practical quantum-inspired applications on room-temperature integrated-circuit chips in the future (e.g., for computational quantum chemistry).

Our work is not meant to be a classical alternative to quantum computation, but complementary and synergistic with it, as in, for example, hybrid quantum and classical systems or in quantum-inspired systems. For example, we have described a "quantum cochlea" (Sarpeshkar, 2019b), a traveling-wave spectrum analyzer inspired by the biological inner ear, that ports ideas from sound spectrum analysis, a classical nonlinear fluid-membrane-distributed analog computation, to electromagnetic spectrum analysis, a quantum analog computation with distributed WKB-like traveling waves, that is, effectively a slow-wavelength-varying Schrodinger-like equation with loss. Thus, we can create quantum-inspired and bio-inspired spectrum analysis, leveraging the power of computation in nature, in both physics and in biology.

In summary, we have shown that four novel complex-voltage/complex-current analog-circuit parts can reformulate and architect unitary and coherent quantum-inspired dynamical systems in an easily scalable, modular, and broadband fashion for any $N \times N$ Hamiltonian. Classical emulations and instantiations of these parts with paired-real-value circuits enable any $N \times N$ quantum Hamiltonian to be mapped to an equivalent $2N \times 2N$ classical one. Theoretically and on a silicon integrated-circuit chip, we also show that tensor-product and QFT computations on 2^n simultaneously superposed states can be implemented with $O(n)$ of these parts. Our work may help build a circuit bridge between quantum and neural computation, both of which exploit analog computation, whether with complex numbers or with real numbers, respectively.

Acknowledgments

We acknowledge useful discussions with M. Blencowe. This work was supported by a grant from the Office of Naval Research (grant N00014-19-1-2434) to R. Sarpeshkar. W. Wattanapanitch was supported by a contract to Dartmouth College under the supervision of R. Sarpeshkar.

Author Contributions

A.C. performed Matlab and circuit simulations; analyzed experimental data; helped write, review, and revise the paper; and contributed to the conception and implementation of mathematical results. W.W. designed and implemented the chip in consultation with R.S., performed experiments on it, gathered experimental data from the chips, helped write the paper, and helped with circuit and Matlab simulations. I.C. helped review the paper, write it, and provided important theoretical and experimental knowledge for the limitations and context of quantum versus quantum-inspired computing. R.S. invented the analog circuit formulation, emulation, and underlying theory; helped design the chip; helped with circuit and Matlab simulations, helped write the paper, helped develop the mathematical results, and supervised the overall project.

Competing Interests

R.S. discloses that he is the sole inventor on four awarded patents related to this work, on which it is founded. They are cited in the References.

Data and Materials Availability

All data relevant to work described in this letter are available in the main text.

References

Arute, F., Arya, K., Babbush, R., Bacon, D., Bardin, J. C., Barends, R., . . . Martinis, J. M. (2019). Quantum supremacy using a programmable superconducting processor. *Nature*, *574*, 505–510. 10.1038/s41586-019-1666-5, PubMed: 31645734

Borders, W. A., Pervaiz, A. Z., Fukami, S., Camsari, K. Y., Ohno, H., & Datta, S. (2019). Integer factorization using stochastic magnetic tunnel junctions. *Nature*, *573*, 390–393. 10.1038/s41586-019-1557-9, PubMed: 31534247

Budzinski, R. C., Nguyen, T. T., Đoàn, J., Mináč, J., Sejnowski, T. J., & Muller, L. (2021). *The geometry of transient dynamics for synchronization and chimera states*. Manuscript in preparation.

Cohen, L., Brady, A., Huang, Z., Liu, H., Qu, D., Dowling, J., & Han, M. (2021). Efficient simulation of loop quantum gravity: A scalable linear-optical approach. *Phys. Rev. Lett.*, *126*, 020501. 10.1103/PhysRevLett.126.020501

Czischek, S., Baumbach, A., Billaudelle, S., Cramer, B., Kades, L., Pawlowski, J. M., . . . Gärttner, M. (2021). *Spiking neuromorphic chip learns entangled quantum states*. arXiv:2008.01039.

Feynman, R. P. (1982). Simulating physics with computers. *Int. J. Theor. Phys.*, *21*, 467–488. 10.1007/BF02650179

Feynman, R. P., Leighton, R. B., & Sands, M. L. (2011). *The Feynman lectures on physics*, vol. *3*. New York: Basic Books.

Fukami, S., Borders, W. A., Pervaiz, A. Z., Camsari, K. Y., Datta, S., & Ohno, H. (2020). Probabilistic computing based on spintronics technology. In *Proceedings of the 2020 IEEE Silicon Nanoelectronics Workshop* (pp. 21–22). Piscataway, NJ: IEEE. 10.1109/SNW50361.2020.9131622

Gilyén, A., Su, Y., Low, G., & Wiebe, N. (2019). Quantum singular value transformation and beyond: Exponential improvements for quantum matrix arithmetics. In *Proceedings of the 51st Annual ACM SIGACT Symposium on Theory of Computing* (pp. 193–204). New York: ACM.

Grover, L. (1996). A fast quantum mechanical algorithm for database search. In *Proceedings of the Twenty-Eighth Annual ACM Symposium on Theory of Computing* (pp. 212–219). New York: ACM.

Hahnloser, R., Sarpeshkar, R., Mahowald, M., Douglas, R. J., & Seung, H. S. (2000). Digital selection and analogue amplification coexist in a cortex-inspired silicon circuit. *Nature*, *405*, 947–951. 10.1038/35016072, PubMed: 10879535

Huang, Y., Guo, N., Seok, M., Tsividis, Y., & Sethumadhavan, S. (2016). Evaluation of an analog accelerator for linear algebra. In *Proceedings of the 43rd International Symposium on Computer Architecture* (pp. 570–582). Piscataway, NJ: IEEE.

Kim, J., Woo, S. S., & Sarpeshkar, R. (2018). Fast and precise emulation of stochastic biochemical reaction networks with amplified thermal noise in silicon chips. *IEEE Transactions on Biomedical Circuits and Systems*, *12*, 379–389. 10.1109/TBCAS.2017.2786306, PubMed: 29570064

Kish, L. (2003). Quantum computing with analog circuits: Hilbert space computing. In *Proceedings of SPIE 5055, Smart Structures and Materials 2003: Smart Electronics, MEMS, BioMEMS, and Nanotechnology*. SPIE. 10.1117/12.497438

Kuramoto, Y. (1984). Cooperative dynamics of oscillator community: A study based on lattice of rings. *Progress of Theoretical Physics Supplement*, *79*, 223–240. 10.1143/PTPS.79.223

La Cour, B. R., Ostrove, C. I., Ott, G. E., Starkey, M. J., & Wilson, G. R. (2016). Classical emulation of a quantum computer. *International Journal of Quantum Information*, *14*(4) 1640004. 10.1142/S0219749916400049

Lee, D., & Seung, H. (1999). Learning the parts of objects by non-negative matrix factorization. *Nature*, *401*, 788–791. 10.1038/44565, PubMed: 10548103

Mead, C. (1989). *Analog VLSI and neural systems*. Reading, MA: Addison-Wesley.

Nielsen, M., & Chuang, I. (2010). *Quantum computation and quantum information: 10th anniversary edition*. Cambridge: Cambridge University Press.

Pedroni, B. U., Deiss, S. R., Mysore, N., & Cauwenberghs, G. (2020). Design principles of large-scale neuromorphic systems centered on high bandwidth memory. In *Proceedings of the 2020 International Conference on Rebooting Computing* (pp. 90–94). Piscataway, NJ: IEEE. 10.1109/ICRC2020.2020.00013

Sarpeshkar, R. (1998). Analog versus digital: Extrapolating from electronics to neurobiology. *Neural Computation*, *10*(7), 1601–1638. 10.1162/089976698300017052, PubMed: 9744889

Sarpeshkar, R. (2010). *Ultra low power bioelectronics: Fundamentals, biomedical applications, and bio-inspired systems*. Cambridge: Cambridge University Press.

Sarpeshkar, R. (2019a). *Emulation of quantum and quantum-inspired spectrum analysis and superposition with classical transconductor-capacitor circuits*. U.S. Patent No. 10,204,199. Washington, DC: U.S. Patent and Trademark Office.

Sarpeshkar, R. (2019b). *Quantum cochlea for efficient spectrum analysis*. U.S. Patent No. 10,248,748. Washington, DC: U.S. Patent and Trademark Office.

Sarpeshkar, R. (2019c). *Emulation of quantum and quantum-inspired discrete-state systems with classical transconductor-capacitor circuits*. U.S. Patent No. 10,275,556. Washington, DC: U.S. Patent and Trademark Office.

Sarpeshkar, R. (2020). *Emulation of quantum and quantum-inspired dynamical systems with classical transconductor-capacitor circuits*. U.S. Patent No. 10,769,388. Washington, DC: U.S. Patent and Trademark Office.

Sarpeshkar, R., & O'Halloran, M. (2002). Scalable hybrid computation with spikes. *Neural Computation*, *14*, 2003–2038. 10.1162/089976602320263971, PubMed: 12184840

Shor, P. W. (1994). Algorithms for quantum computation: Discrete logarithms and factoring. In *Proceedings of the 35th Annual Symposium on Foundations of Computer Science* (pp. 124–134). Piscataway, NJ: IEEE. 10.1109/SFCS.1994.365700

Teo, J. Y., & Sarpeshkar, R. (2020). The merging of biological and electronic circuits. *iScience*, *23*(11), 101688.

Traversa, F. L., Ramella, C., Bonani, F., & Di Ventra, M. (2015). Memcomputing NP-complete problems in polynomial time using polynomial resources in collective states. *Science Advances*, *1*, e1500031. 10.1126/sciadv.1500031, PubMed: 26601208

Wang, Z., Joshi, S., Savel'ev, S., Jiang, H., Midya, R., Lin, P., . . . Yang, J. J. (2017). Memristors with diffusive dynamics as synaptic emulators for neuromorphic computing. *Nature Mater*, *16*, 101–108. 10.1038/nmat4756

Weinstein, S. (2021). *Boltzmann machines as thermal models for quantum systems*. arXiv:1807.03910. http://arxiv.org/abs/1807.03910

Whitfield, J. D., Biamonte, J., & Aspuru-Guzik, A. (2011). Simulation of electronic structure Hamiltonians using quantum computers. *Molecular Physics*, *109*(5), 735–750. 10.1080/00268976.2011.552441

Woo, S. S., Kim, J., & Sarpeshkar, R. (2018). A digitally programmable cytomorphic chip for simulation of arbitrary biochemical reaction networks. *IEEE Transactions on Biomedical Circuits and Systems*, *12*(2), 360–378. 10.1109/TBCAS.2017.2781253, PubMed: 29570063

Woo, S. S., & Sarpeshkar, R. (2013). A spiking-neuron collective analog adder with scalable precision. In *Proceedings of the 2013 IEEE International Symposium on Circuits and Systems* (pp. 1620–1623). Piscataway, NJ: IEEE. 10.1109/ISCAS.2013.6572172

Xiao, M., Martin, I., Yablonovitch, E., & Jiang, H. W. (2004). Electrical detection of the spin resonance of a single electron in a silicon field-effect transistor. *Nature*, *430*, 435–439. 10.1038/nature02727, PubMed: 15269763

Yamamoto, Y., Leleu, T., Ganguli, S., & Mabuchi, H. (2020). Coherent Ising machines: Quantum optics and neural network perspectives. *Applied Physics Letters*, *117*, 160501. 10.1063/5.0016140

Received September 8, 2021; accepted November 15, 2021.